Deformation profiles and microscopic dynamics of complex fluids during oscillatory shear experiments

Electronic Supplementary Information

Paolo Edera,[a] Matteo Brizioli,[a] Giuliano Zanchetta,[a] George Petekidis,[b] Fabio Giavazzi,[a] and Roberto Cerbino*[a,c]

1 Image processing algorithms

1.1 Global displacement tracking

We describe here the global displacement tracking algorithm that we use for the calibration of the oscillation frequency, for the characterization of the deformation field, and for the registration of sample drifts, including apparent ones due to synchronizations errors.

The first step of the analysis consists in subtracting a background image $I_B(\mathbf{x}) = I_B(x,y)$ from the entire stack of images. $I_B(\mathbf{x})$ is estimated as the temporal average $I_B(\mathbf{x}) = \langle I(\mathbf{x},t)\rangle_t$ of an experimental acquisition performed imposing to the sample a deformation amplitude large enough that the signal associated with the particles is completely averaged out, and only static features remain, which are typically due to undesired objects (e.g. dust particles on the camera sensor or the optics) in the optical path.

The displacement between two consecutive background-corrected images is then estimated by locating the position of the maximum of the spatial correlation function

$$c(x,y,t,t+\Delta t) = \Sigma_{x_0,y_0} I_t(x_0,y_0) I_{t+\Delta t}(x_0+x, y_0+y). \qquad (1)$$

Ideally, a simple shear deformation acts on each shear-vorticity plane as a rigid translation in the shear direction. As a result, neglecting finite-size effects (a reasonable assumption as long as the displacement is smaller than half of the image size) and out-of-plane contributions, an image of a sheared sample collected at time $t+\Delta t$ is simply a translated version of the image at time t $I_{t+\Delta t}(x) = I_t(x+\Delta x, y+\Delta y)$. In this case, the correlation function $c(x,y,t,t+\Delta t)$ is expected to display a sharp peak centered around $(x,y) = -(\Delta x, \Delta y)$ (see Fig.S1). The spatial correlation function in Eq.1 can be efficiently computed in the Fourier space, since the convolution product simplifies to an algebraic product

$$c(\mathbf{x},t,t+\Delta t) = \mathscr{F}^{-1}\{\hat{I}_t(\mathbf{q})\hat{I}^*_{t+t_0}(\mathbf{q})\}. \qquad (2)$$

Once we obtain the spatial correlation function between two images, we identify the position (x_M, y_M) of the absolute maximum. To reach sub-pixel precision, we consider the projection of the correlation function on one axis (say, the x-axis) in a neighborhood of the maximum:

$$\bar{c}(x) = \Sigma_{y=y_M-\delta}^{y_M+\delta} c(x,y), \qquad (3)$$

where the half-amplitude δ of the considered interval along the orthogonal direction y is set to $\delta = 4$ pixels. A Gaussian is then fitted to the obtained mono-dimensional profile

$$\bar{c}(x) = a \cdot e^{-(x-\tilde{x}_M)^2/2\sigma^2} + d. \qquad (4)$$

leading to the improved estimate $\tilde{x}_M$ of the maximum position. The same procedure can be repeated along the orthogonal direction to get an improved estimate of the y-coordinate $\tilde{y}_M$ of the maximum of the spatial correlation function. The sequence of maximum positions $\tilde{\mathbf{x}}_M(t)$ can be used to build the displacement field $\Delta\mathbf{X}(t)$ of the observed plane as function of time: $\Delta\mathbf{X}(t) = \sum_{t'\le t} \tilde{\mathbf{x}}_M(t')$.

For the characterization of the strain field and for the frequency calibration, $\Delta\mathbf{X}(t)$ is fitted with a sinusoidal function. For echo-DDM processing, we acquire m_φ images per period, and we consider m_φ separated stacks. The algorithm is applied to each stack to measure the combination of real and apparent drift for each phase φ. This information is used to minimize the effect of the drift in each echo sequence *via* the stack registration procedure described in the next subsection.

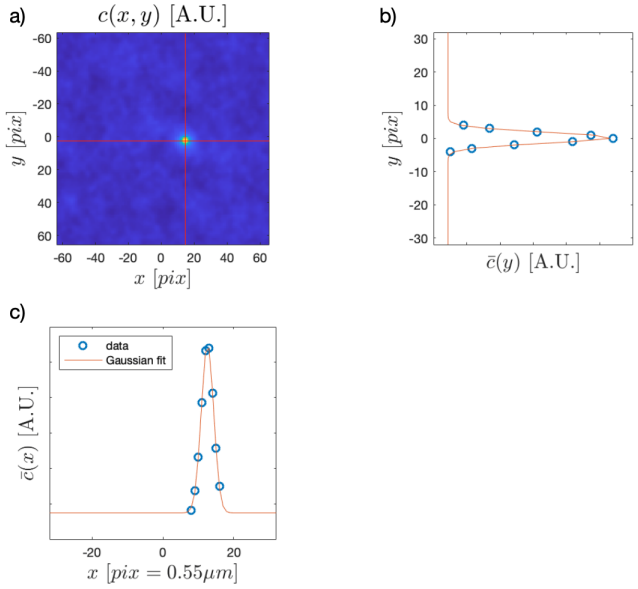

Fig. S1 Global displacement tracking algorithm a) Representative two-dimensional cross-correlation function $c(x,y)$ of two images of a sample under shear collected at different times. The position of the peak (red lines) can be easily identified with single pixel resolution. b,c) Fitting of suitable projections $\bar{c}(y)$ and $\bar{c}(x)$ of $c(x,y)$ on the main axes (symbols) with a Gaussian model enable refining the estimate of the peak position.

[a] *Dipartimento di Biotecnologie Mediche e Medicina Traslazionale, Università degli Studi di Milano, via F.lli Cervi 93, 20090 Segrate, Italy*
[b] *FORTH/IESL and Department of Materials Science and Technology, University of Crete, 71110 Heraklion, Greece*
[c] *University of Vienna, Faculty of Physics, Boltzmanngasse 5, 1090 Vienna, Austria*

1.2 Registration algorithm

Image stack registration consists in correcting each image $I(x,y)$ in the sequence by applying a rigid translation $(\Delta x, \Delta y)$ compensating the (previously determined) drift. Similar to what is done in Ref.[1], this compensation is performed in the Fourier domain *via* the following transformation

$$I(x,y) \longrightarrow e^{j\psi(\Delta x,\Delta y)}\mathscr{F}^{-1}\{M(q_x,q_y)\cdot\mathscr{F}\{I(x,y)\}\}, \qquad (5)$$

where $M(q_x,q_y) = e^{i(q_x\Delta x+q_y\Delta y)}$, $\psi(\Delta x,\Delta y) = \pi(\Delta x+\Delta y-\lfloor\Delta x+\Delta y\rfloor)$, and $\lfloor x\rfloor$ indicates the integer part of x.

The starting image size is 512 x 512 pixels. After registration, only a central portion of each image, of size 384 x 384 pixels, is considered to avoid artifacts at the boundaries.

Before running DDM analysis on the cropped stack, a spatial windowing filter is applied, as described in[2].

2 Synchronization of oscillatory deformation and image acquisition

2.1 Characterization of the oscillation frequency

In our set-up, the shear-cell and the camera are controlled by two different computers. The synchronization of the two devices requires, as a first step, characterizing the frequency of the shear-cell in terms of the clock of the camera's computer. To this end, we performed a series of tests without the sample, measuring the displacement of the top plate under oscillation at the nominal frequency of 1 Hz. By fitting a harmonic function to the displacement, we accurately measure the actual oscillation frequency for different values of the displacement amplitude.

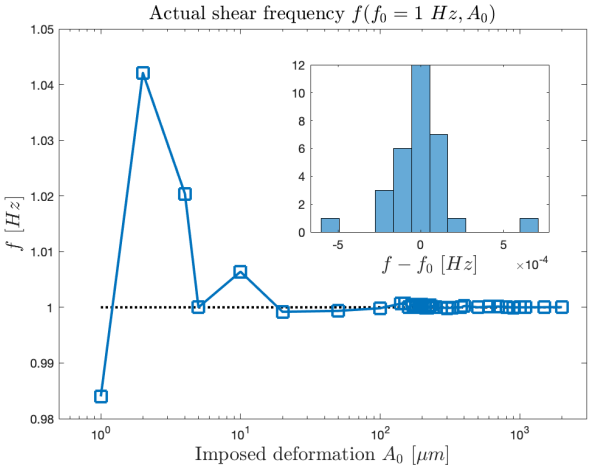

Fig. S2 Actual oscillation frequency. Main panel: Frequency of oscillation as a function of the amplitude for nominal frequency 1 Hz. Inset: histogram of the deviations of single experiment realizations from the mean value $\delta f(A) = f_i(A) - \bar{f}(A)$, the width of the distribution is $\sigma_{\delta f} \sim 10^{-5} Hz$.

In the main panel of Fig.S2, we report $\bar{f}(A)$, the best estimate for the measured oscillation frequency for a given oscillation amplitude A. In the inset, we show the distribution of the frequency $f_i(A)$ measured in different replicas of the same experiments, once subtracted to its mean value $\bar{f}(A)$. The experiment-to-experiment variability can be estimated as the standard deviation $\sigma_{\delta f}$ of the distribution $\sigma_{\delta f} \sim 10^{-5} Hz$.

2.2 Matching the shear-cell frequency and the image acquisition frequency

As described in the main text, our echo protocol requires acquiring m_φ images per period. Once we determine the actual oscillation frequency $\bar{f}(A)$ for a given displacement amplitude A, we must fix the delay time $t_0 = 1/\nu$ between two consecutive images so that it meets the condition $m_\varphi \cdot t_0 = 1/\bar{f}(A)$. The time delay t_0 can be set with a maximum precision of 0.01 ms. For each deformation amplitude A, we choose the optimal pair t_0 and $m_\varphi \in \{4,5,6,7,8\}$ that enables minimizing the rounding error

$$\delta\nu_{round} = |\nu/m_\varphi - \bar{f}(A)|. \qquad (6)$$

The result of this optimization procedure typically provides a rounding error $\delta\nu_{round}/\nu = O(10^{-5})$, which is comparable with the intrinsic variability of $f(A)$ (see previous subsection). The effect of this residual error on the measurements performed on the samples is discussed in the next subsection.

2.3 Residual apparent drift

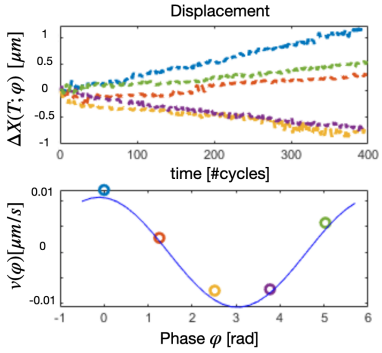

Fig. S3 Apparent Displacement. Top panel: displacement $\Delta X(T;\varphi)$ due to the frequency mismatch, each line correspond to a different starting phase of the oscillation φ. Bottom panel: apparent drift velocity as function of the starting phase φ.

In the top panel of Fig.S3 we report the phase-dependent displacements $\Delta X_\varphi(t)$ measured in a representative experiment on the Sylgard sample subject to an oscillatory deformation with shear amplitude $\gamma_0 = 75\%$. In the bottom panel of Fig.S3 we plot the apparent drift velocity (estimated by fitting a linear model to the curves shown in the upper panel) as a function of the phase φ. Consistently with the discussion reported in Sect. 2.4.3 of the main text, the apparent drift velocity display an harmonic dependence on φ

$$v(\varphi) = V_D \cdot \sin(\varphi+\phi_0) = A(z)\cdot\Delta\omega\cdot\sin(\varphi+\phi_0), \qquad (7)$$

where $A(z)$ is the displacement amplitude on the observed plane and $\Delta\omega$ is the difference between the oscillation frequency and the acquisition frequency, multiplied by 2π. From V_D we can measure the frequency mismatch $\Delta\omega$ associated to the single ex-

periment, and we can compare this value with the one expected according to the previously estimated errors δv_{round} and $\sigma_{\delta f}$. In figure S4 we plot the measured drift velocities V_D (blue symbols) and the one expected from the systematic synchronization errors in both linear (panel a) and semi-logarithmic scale (panel b). A generally good agreement is observed between the experimental drift velocity (blue symbols) and the predicted one (red symbols). In the panel (c) we plot the measured velocity versus the expected one. Over more than two decades in V_P, the accuracy of the prediction is approximately within a factor 2 (marked by light blue dashed lines), and this is due to the intrinsic experiment-to-experiment frequency variability.

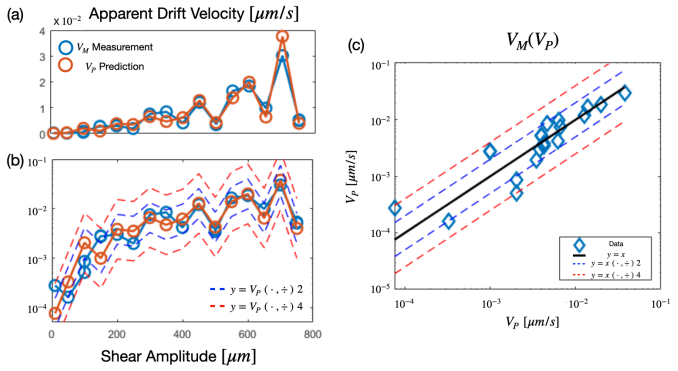

Fig. S4 Prediction of the apparent drift velocity. Panel (a): apparent drift velocity V (as defined in the main text Eq.7) as function of the imposed amplitude (blue symbols). Orange symbols represent the values predicted based on the frequency mismatch. Panel (b): same as (a), where a semi-logarithmic scale is adopted. The region comprised between the blue (orange) dotted lines corresponds to the values compatible with the prediction within a factor of 2 (4). Panel (c): measured drift velocity as function of the predicted one. The dotted lines are as in panel (b).

We conclude that we can quantitatively attribute the residual apparent drift to two causes: the rounding error (due to limited temporal resolution of the camera), and the intrinsic experiment to experiment variability of the actual deformation frequency.

2.4 Residual effect of beat

The registration procedure described above cures the apparent drifts due to synchronization errors in a satisfactory way, yet not perfectly. For sake of completeness, we briefly discuss here also this effect. A more extended treatment can be found in Refs. [1,3]. A small residual contribution due to the frequency mismatch is still visible on the dynamic-structure-functions in the form of an anisotropic pattern. This can be understood by considering the finite depth of focus of the imaging system (sec. 4.1), *i.e.* that an image represent a sort of "projection" of a three-dimensional region on a two-dimensional plane. In other terms, an image does not include only particles lying exactly on the focal plane z_f, but also particles slightly below and above it. If we consider now the effect of these multiple contributions in the light of Eq.7, we find that, since the amplitude depends on the vertical coordinate $A = A(z)$, so does the drift velocity $v(\varphi)$

$$v(\varphi, z) = A(z) \cdot \Delta\omega \cdot \sin(\varphi + \phi_0). \tag{8}$$

As a consequence, in the presence of a non-perfectly synchronized acquisition, the fact that particles on different planes move with slightly different velocity becomes apparent: in fact, the registration effectively removes the displacement of the particles in the focal plane $A(z_f)\sin(\Delta\omega t + \varphi)$, but does not work as well for particles that are out of focus, which exhibit a residual motion.

An estimate of the maximum residual relative velocity between particles that are below the focal plane and those that are above it (i.e. between particles that are at the edges of a region of thickness $2L_f$ centered at the focal plane) is given by (see also Sect.4.1 below):

$$\begin{aligned} v_R(\varphi) = v(\varphi, z_f + L_f) - v(\varphi, z_f - L_f) = \\ \Big(A(z_f + L_f) - A(z_f - L_f)\Big) \cdot \Delta\omega \cdot \sin(\varphi + \phi_0) = \\ 2\gamma(z_f) L_f \cdot \Delta\omega \cdot \sin(\varphi + \phi_0). \end{aligned} \tag{9}$$

The residual drift velocity v_R does not depend on the vertical coordinate of the focal plane but only on $\gamma(z_f)$ and on the depth of focus L_f. We also note that using equations 7 and 9, it is possible to express v_R as a function of the focal plane apparent displacement v_D: $v_R = \alpha v_D$, where $\alpha = 2\gamma(z_f)L_f/A(z) = 2L_f/z_f$. Since $L_f \sim O(10)\mu m$ (see Sect.4.1 below), and the focal plane coordinate $z_f = 250\ \mu m$, the factor α is of order 0.1, which is compatible with the results in Fig. 6 of the main text.

3 Real Drifts

In Fig.S5 we report the absolute value of the measured drift velocity for the four samples considered in this study. As expected, the drift velocity V for the elastic sample (Sylgard) is negligible ($V < 5nm/s$), and almost independent of the shear amplitude. In all the other samples, we do observe a small net flow, whose velocity depends on the shear amplitude. For the fluid-like samples, the drift velocity attains a finite value at small shear amplitudes, while for the yield stress fluid (Carbopol) the drift velocity quickly drops to values comparable with the solid sample as the amplitude is reduced.

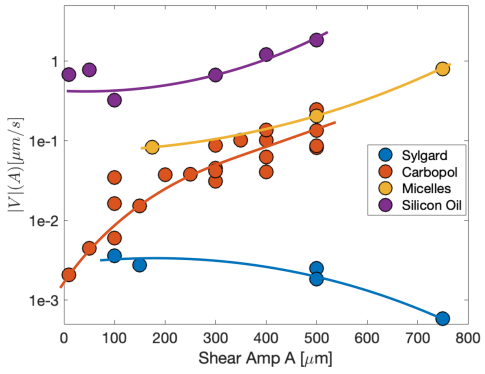

Fig. S5 Drift velocities. Symbols: absolute values of the estimated drift velocities measured for the four sample considered in this study as a function of the amplitude of the displacement imposed on the moving plate. Lines are guidelines for the eyes.

4 Microscopy set-up

4.1 Depth-of-focus

The depth of focus (DOF) of an imaging system is the minimum vertical displacement Δz along the optical axis direction to obtain an image that is no longer significantly correlated with the initial one. This concept can be made more precise by adopting different specific correlators, either in real or reciprocal space[3,4]. Working in the Fourier space has the advantage that, as long as the image-forming process is linear, each spatial mode decorrelates independently of the others and this enables estimating a wavevector-dependent DOF which is independent of the specific spectral content of the image. From a stack of images acquired at different vertical coordinates z in static sample, we consider the following correlation function

$$c(q,\Delta z) = \frac{\langle \hat{I}(\mathbf{q},z_0)\cdot \hat{I}^*(\mathbf{q},z_0-\Delta z)\rangle_{|\mathbf{q}|=q}}{|\tilde{I}(\hat{\mathbf{q}},z_0)|^2}, \tag{10}$$

where z_0 identifies the plane where the Kohler illumination condition is realized[4], chosen to be in the middle of the gap: $z_0 = h/2$. Fitting an exponential function to each of the correlation functions in Eq.10 enables extracting for each q-value an estimate of the correlation length, which provides an estimate for the q-resolved DOF $L_f(q)$. In Fig.S6 we report the obtained $L_f(q)$ for two different illumination conditions: completely open (red symbols) and completely closed (blue symbols) aperture diaphragm. The sample is the same elastomer (Sylgard) with embedded tracer particles used in the experiments described in the main text. As expected, the DOF decreases more rapidly with q as the size of the aperture diaphragm is increased. The range of

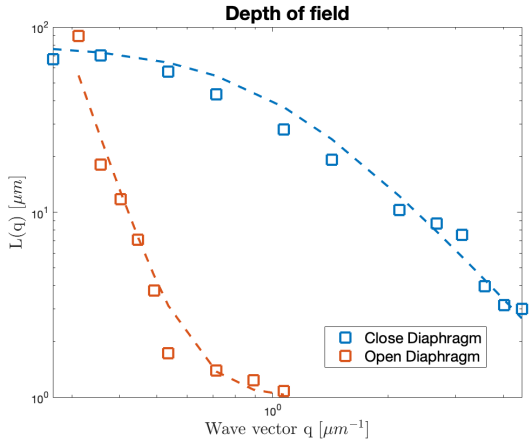

Fig. S6 Experimental determination of the depth of focus (DOF) of the opticola system. Symbols: q-resolved DOF $L_f(q)$ measured with closed (blue symbols) and opened (red symbols) aperture diaphragm. The dashed lines are guide At small wave-vectors the estimated DOF saturates to a plateau value due to the finite gap width h.

wave-vectors considered in the experiments is typically $[0.2,3]$ μm^{-1}. In the completely open diaphragm case, which corresponds to the working condition adopted in our experiments, for $q > 0.3\ \mu m^{-1}$ the correlation length is always shorter than 20 μm, rapidly falling below 2 μm for $q > 0.5\ \mu m^{-1}$.

4.2 Alignment of the confining plates

The accurate characterization of the microscopic state of a sample under macroscopic shear requires an extremely precise control on the mechanical conditions. To produce a simple shear deformation in our parallel plate geometry, two basic requirements must be fulfilled: the two plates must be parallel, and the translation of the moving plate must take place without variations in the distance between the plates. In this subsection, we describe the adopted two-step alignment procedure.

In the first step, in the absence of any samples, the vertical position of the objective is adjusted in such a way to provide a sharp image of the top moving slide, defining the reference position z_0. Then, a displacement of $\pm$1mm is imposed on the slide. By using the graduated scale on the knob controlling the vertical position of the objective, we measure the amplitude $\Delta z = |z_+ - z_-|$ of the displacement of the slide along the optical axis. We then recursively act on the micrometric screws described in Ref.[5] to adjust the orientation of the slide. A satisfactory alignment is obtained when $\Delta z < 2\mu m$. In this condition, when a strain $\gamma_0 = 200\%$ is imposed on a sample of thickness $h = 500\ \mu m$, the maximum spurious sample compression (expansion) corresponds to a normal strain $\varepsilon = \Delta z/h = 0.2\%$.

The second step is aimed at making the bottom plate parallel to the top one. To this end, we orient the position of the bottom plane through the built-in system of screws, and we monitor the angle between the two plates with an interferometric system. We adopt here an interferometric technique similar to the one described in Ref.[6], adapted to ensure compatibility with the microscope ports. A very simple implementation, which however requires removing all the lenses present along the optical path of the microscope, is the following. A collimated laser beam of wavelength λ_L is sent through the microscope back-port (which is normally used for epi-illumination), it is reflected by the beam splitter and impinges on the two plates. Two reflected beams are generated, which are reflected again by the beam splitter toward the camera sensor, where they produce an interference pattern. If the slides are tilted by an angle θ_x, the camera detects a pattern of fringes with wavelength $\Lambda_x \sin(\theta_x) = \lambda_L/2$. Using the micrometric screws we adjust the orientation of the bottom plate with the aim of maximizing Λ_x. We obtain the best alignment when the fringes are no longer visible, *i.e.* when Λ_x exceeds the sensor size:

$$\Lambda_x > \text{sensor size } = 1\ mm, \tag{11}$$

which means that $\theta_x \leq \lambda_L/\Lambda_x = 2\cdot 10^{-3}$rad. In our experiments, we opt for a slightly different implementation that does not require removing any element from the optical path of the microscope. We use a low magnification objective (2x) and insert a suitable diverging lens close to the microscope back-port in order to obtain, at least approximately, a collimated illumination of the shear-cell plates. The microscope objective introduces a magnification factor $M = 2$ in the collected diffraction pattern, leading to a two-fold reduction in the size of the accessible field of view $\Lambda_x \longrightarrow \Lambda_x' = \Lambda_x/2$. According to the argument sketched above, in this configuration the alignment accuracy can be thus estimated as $\theta_x' = \lambda_L/\Lambda_x' \leq 4\cdot 10^{-3}$rad.

5 Stationarity of the deformation profile

For all the samples considered in this study, the stationarity of the deformation profile during a single experiment (whose typical duration is 400 s) was checked by repeating multiple times (at least three) the z-scan procedure described in Sect. 2.3 of the main text. In the Fig.S7, we report the results of three z-scans, performed in quick succession on the Sylgard sample under an oscillatory shear deformation with strain amplitude $\gamma_0 = 75\%$. As it can be appreciated, the three scans are almost indistinguishable, confirming the absence of time evolution in the deformation profile over the investigated time window, and the good reproducibility in the vertical positioning of the objective, which is controlled by a rotating wheel equipped with a graduated scale. Similar results

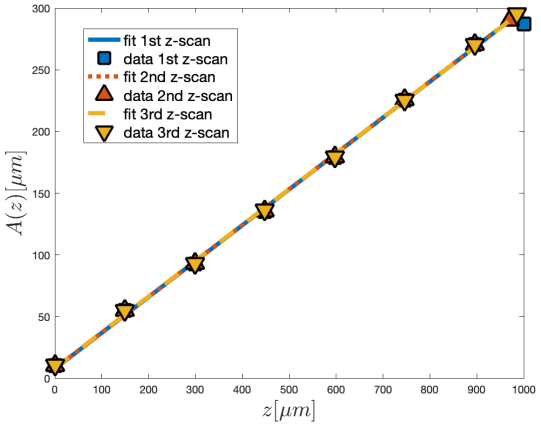

Fig. S7 Stationarity of the deformation profile. Symbols: reconstructed displacement profiles in the Sylgard sample, obtained from three independent measurements performed in quick succession during an oscillatory shear experiment. Lines are best fitting curves with a linear model.

holds for the other samples.

6 Rheological characterization of the Carbopol sample

The Carbopol sample considered in this study exhibits the typical yield stress fluid-response to an oscillatory perturbation, as confirmed by an amplitude sweep experiment performed with an Anton-Paar (MCR301) rheometer at an oscillation frequency of 1 Hz (Fig.S8). The yield strain, estimated as the strain amplitude at which the storage and the loss moduli become equal[7–9] is about 60%, while the onset of non-linear response occurs for $\gamma_0 > 2-3\%$.

7 Tracer dynamics in the Carbopol sample at rest

Even in the absence of external forcing, PS2 tracer particles dispersed in the Carbopol exhibit a non-negligible, although extremely slow, dynamics that we characterized with standard DDM. Over the time window $[1-100]$ s considered in our experiment, the ISFs are far from reaching a complete decorrelation, as it can be appreciated from Fig.S9.

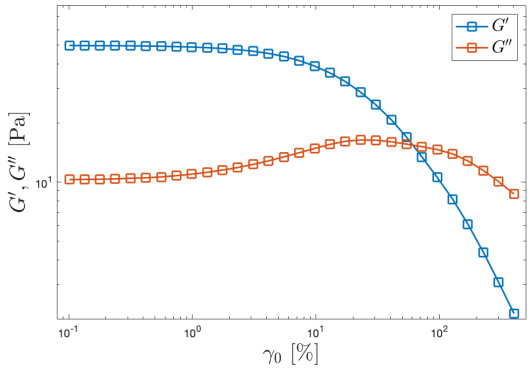

Fig. S8 Amplitude sweep experiment on the Carbopol sample. Storage and loss moduli $G'(\gamma), G''(\gamma)$ are plotted as a function of the imposed strain amplitude γ_0. We can identify a linear region where the viscoelastic moduli are independent on the shear amplitude ($\gamma_0 < 1\%$), a wide transition region where the response is still dominated by the elastic modulus and the moduli depends on the shear amplitude ($1\% < \gamma_0 < 60\%$), a terminal "fluid-like" region where the response is dominated by the loss modulus ($\gamma_0 > \gamma_C \simeq 60\%$).

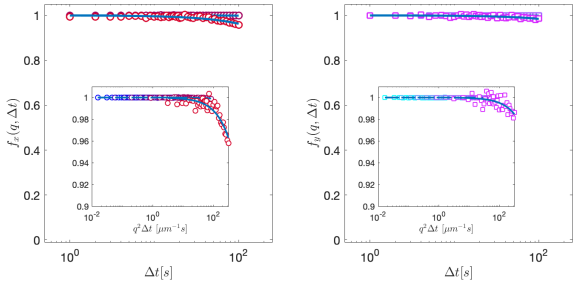

Fig. S9 Tracer dynamics at rest in Carbopol. Symbols: representative ISFs for different q-values in the range $[0.15-2.2]\mu m^{-1}$ along two perpendicular directions x (left), y (right). Continuous lines are best fitting curves with the model $f_i(q,\Delta t) = e^{-\Gamma(q)\Delta t}$. In the insets the ISFs are plotted as a function of $q^2\Delta t$. The good overlap of the rescaled intermediate scattering functions suggest compatibility with a very slow diffusive dynamics.

The fact that only a small fraction of the decay of the ISFs is observed for all accessible q-values makes the estimate of the corresponding diffusion coefficient D_{rest} extremely noisy. Fitting the model $f_i(q,\Delta t) = e^{-\Gamma(q)\Delta t}$ to the data provides the value $D_{rest} \simeq (1.5 \pm 1) \cdot 10^{-5} \mu m^2/s$. Within the experimental error, the tracer dynamics is identical along the two considered directions.

Notes and references

1 J. A. Richards, V. A. Martinez and J. Arlt, *Soft Matter*, 2021, **17**, 3945–3953.

2 F. Giavazzi, P. Edera, P. J. Lu and R. Cerbino, *The European Physical Journal E*, 2017, **40**, 1–9.

3 S. Aime and L. Cipelletti, *Soft matter*, 2019, **15**, 213–226.

4 F. Giavazzi, D. Brogioli, V. Trappe, T. Bellini and R. Cerbino, *Physical Review E*, 2009, **80**, 031403.

5 J.-B. Boitte, C. Vizcaïno, L. Benyahia, J.-M. Herry, C. Michon and M. Hayert, *Review of Scientific Instruments*, 2013, **84**, 013709.

6 S. Aime, L. Ramos, J.-M. Fromental, G. Prevot, R. Jelinek and L. Cipelletti, *Review of Scientific Instruments*, 2016, **87**, 123907.
7 M. Dinkgreve, J. Paredes, M. M. Denn and D. Bonn, *Journal of non-Newtonian fluid mechanics*, 2016, **238**, 233–241.
8 N. Koumakis, A. Pamvouxoglou, A. Poulos and G. Petekidis, *Soft Matter*, 2012, **8**, 4271–4284.
9 N. J. Wagner and J. Mewis, *Theory and Applications of Colloidal Suspension Rheology*, Cambridge University Press, 2021.